ACS Energy LETTERS

http://pubs.acs.org/journal/aelccp

Letter

Structural Evolution and Thermal Behavior of High-Ni Cathodes: Coupled Operando XAS, XRD, and Mass Spectrometry Analysis

Yuying Zhang, Chao Wang, Jihao Zhang, Hanwei Liu, Jianwen Wang, Zhenzhong Li, Wencheng Su, Wei Zhou, Wenbo Zhai, Jiahe Zang, Shaofei Wang,* Qingyu Kong,* and Chunzhen Yang*

Cite This: *ACS Energy Lett.* 2026, 11, 3936−3944

Read Online

ACCESS | Metrics & More | Article Recommendations | Supporting Information

ABSTRACT: Understanding the intrinsic thermal instability of Ni-rich cathodes is critical for elucidating the thermal runaway mechanisms in lithium-ion batteries. Here, we investigate the thermally induced decomposition of Ni-rich cathodes under electrolyte-free conditions using time-resolved operando approaches, including X-ray diffraction (XRD), X-ray absorption spectroscopy (XAS), and online mass spectrometry (OMS). The results reveal a coupled evolution of oxygen release, Ni redox, and structural transformations during heating. Oxygen release is initiated prior to detectable bulk phase transition and correlates with early structural disorder, as tracked by the evolution of the $(003)_L$ and $(104)_L$ reflections. Deep delithiation at 4.8 V (∼95% SOC) accelerates Ni reduction and amplifies structural instability, leading to approximately 3-fold higher early stage oxygen release compared with the 4.3 V (∼85% SOC) condition. These findings establish a coupling-based framework for understanding cathode-driven thermal instability and provide guidance for improving battery safety.

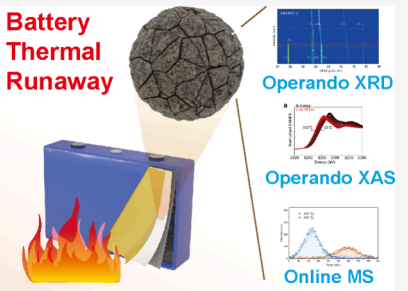

With the rapid development of electric vehicles and energy storage devices, higher demands are placed on the energy density, power density, safety performance, and cycle life of lithium-ion batteries (LIBs).[1] Among these, thermal stability remains a major bottleneck in the development of high-energy-density batteries. Under extreme conditions such as overcharging,[2,3] external short circuits,[4,5] high temperatures,[6,7] or mechanical damage,[8,9] thermal runaway (TR) may be triggered, leading to combustion or even explosions, thereby posing serious safety risks to the battery system. Nevertheless, the intrinsic thermal instability of cathode materials plays a critical role, as its decomposition provides both oxygen release and heat generation that drive and sustain the TR process.

High-nickel layered oxides ($LiNi_xCo_yMn_{1-x-y}O_2$, $x \geq 0.8$, denoted as NCM) have been widely adopted in high-energy-density lithium-ion batteries because of their high specific capacity and relatively low cost.[10−12] However, their intrinsically poor thermal stability remains a critical challenge.[13−15] Extensive studies have shown that Ni-rich NCM cathodes undergo pronounced structural degradation accompanied by oxygen release at elevated temperatures, a process typically initiating at ∼180 °C and termed the critical T_1 stage.[16−18] Recent computational and experimental investigations indicate that this oxygen release is driven by lattice oxygen oxidation coupled with Ni migration to Li sites, which induces severe cation disorder and ultimately leads to structural collapse.[19,20] Notably, these structural and thermal instabilities are highly sensitive to both the Ni content and the degree of delithiation.[21−23] Moreover, the onset temperatures and kinetic characteristics of these transformations vary substantially with Ni concentration, particle morphology, and surface chemistry, underscoring the complex interplay between composition, structure, and thermal behavior in Ni-rich NCM cathodes.[24−26] Therefore, a comprehensive understanding of their structural evolution and oxygen-release mechanisms under thermal stress is essential for the rational design of thermally robust high-Ni cathode materials.

Although a variety of characterization techniques—including differential scanning calorimetry (DSC), thermogravimetric analysis (TGA), operando X-ray diffraction (XRD), and gas chromatography−mass spectrometry (GC−MS)—have been employed to investigate the thermal runaway (TR) behavior of cathode materials;[27−31] these methods are typically applied independently. Consequently, correlating structural evolution, electronic-state changes, and gas release in a unified and time-resolved manner remains a significant challenge. Establishing these precise correlations, which requires the simultaneous acquisition and integration of multiple data streams, is essential for constructing a comprehensive and mechanistic understanding of the TR process.

To address this limitation, this study proposes an integrated operando approach that combines *operando* XRD and/or X-ray absorption spectroscopy (XAS) with online mass spectrometry (OMS). As illustrated in Scheme 1, this configuration enables

Received: February 6, 2026
Revised: March 21, 2026
Accepted: April 2, 2026
Published: April 7, 2026

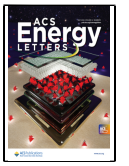

Scheme 1. (a) Schematic Illustration of the Thermal Decomposition Process of High-Ni NCM Cathode Materials; (b) Scheme of the *operando* XRD/XAS-OMS Test Protocol

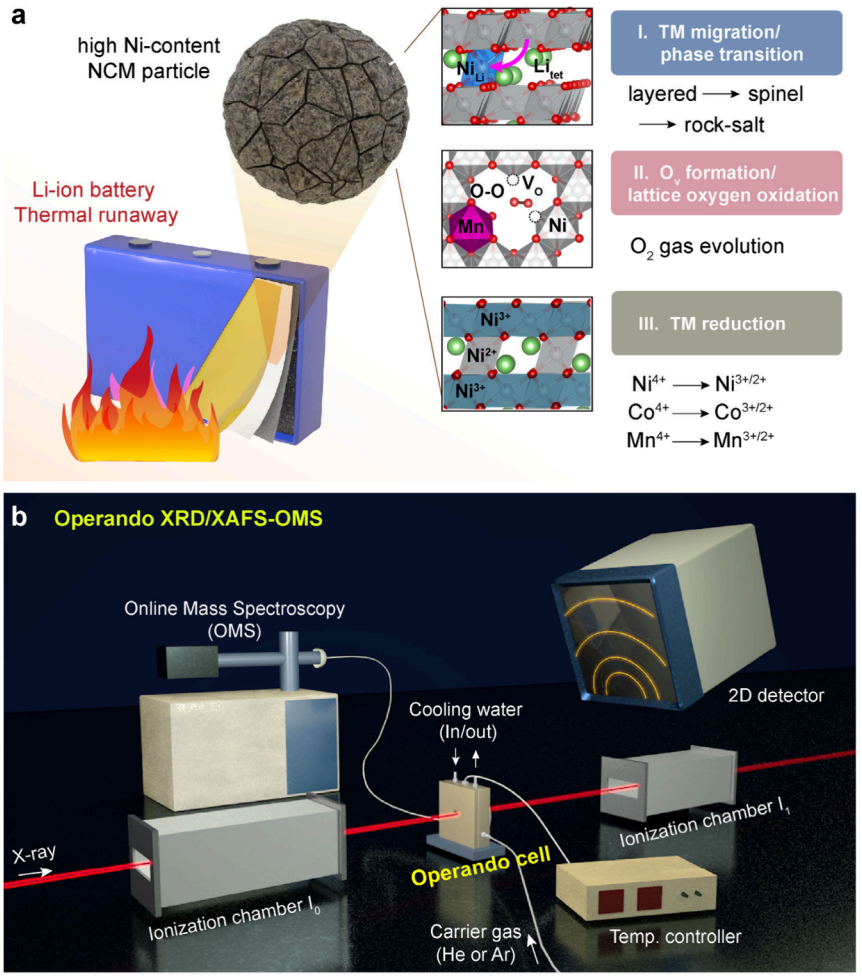

real-time, synchronized monitoring of structural and gas-evolution processes under identical conditions, allowing direct correlation between phase transitions, transition-metal redox, and oxygen release. In this study, we focus on the intrinsic thermal decomposition behavior of the cathode under electrolyte-free conditions, aiming to isolate the cathode-driven contributions to thermal runaway. To demonstrate this experimental protocol, the evolution of transition-metal valence states is primarily derived from Ni K-edge XANES measurements.

$LiNi_{0.8}Co_{0.1}Mn_{0.1}O_2$ (NCM811) exhibits diffraction patterns characteristic of the α-$NaFeO_2$-type layered structure with an *R*-3*m* space group (Figure 1).[32] Scanning electron microscopy (SEM) reveals polycrystalline secondary particles with granular morphologies and an average particle size of ~10 μm (Figure S2).[33] Electrochemical evaluation shows that, at a current density of 0.33 C, the NCM811 electrode delivers a first-discharge capacity of ~200 mAh g^{-1}. The differential capacity (dQ/dV) profiles (Figure S3) display typical H1−M−H2 transitions below 4.2 V and an H2−H3 transition above 4.3 V, consistent with previous reports.[34,35] These results confirm that the material exhibits representative electrochemical behavior.

In this study, we focus on the intrinsic thermal decomposition behavior of the cathode under electrolyte-free conditions, aiming to isolate the cathode-driven contributions to thermal runaway. For thermal analysis, the cathode was charged to 4.3 V to reach delithiated state (denoted as d-NCM811, ~85% delithiation). To isolate intrinsic cathode-driven processes, *operando* XRD-OMS and XAFS experiments were conducted under electrolyte-free conditions. A sharp $(003)_L$ diffraction peak appears at ~18.7° upon charging to 4.3 V. During subsequent thermal annealing, this peak remains stable up to ~190 °C, above which it gradually weakens and shifts slightly (Figure 1c). Simultaneously, the emergence of the $(111)_S$ peak indicates the formation of a spinel phase.[36] OMS reveals a two-stage O_2 evolution with peak temperatures at ~205 and ~300 °C. These two events, denoted as T_1 and T_2, correlate well with the layered H3 → spinel and spinel → rock-salt phase transitions observed via *operando* XRD.[37] The ratio of O_2 released during the T_1 and T_2 stages (O_{T1}/ O_{T2}) is ~1:1 (Figure S7).

To further quantify the structural evolution, the temperature-dependent intensities of the $(003)_L$ (Figure 1d) and $(104)_L$ (Figure 1e) diffractions were extracted from the full *operando* XRD patterns. These two characteristic peaks provide a sensitive probe of layered structure integrity and cation distribution. Here, we focus on the T_1 event, as it governs the early stage thermal instability. As shown in Figure 1f, both peak intensities decrease sharply near ~190 °C, coinciding with the onset of oxygen release, indicating a strong correlation between structural degradation and oxygen evolution.

The $I(003)/I(104)$ intensity ratio is used here as a qualitative indicator of Li/Ni cation mixing within the temperature range

https://doi.org/10.1021/acsenergylett.6c00367
ACS Energy Lett. 2026, 11, 3936−3944

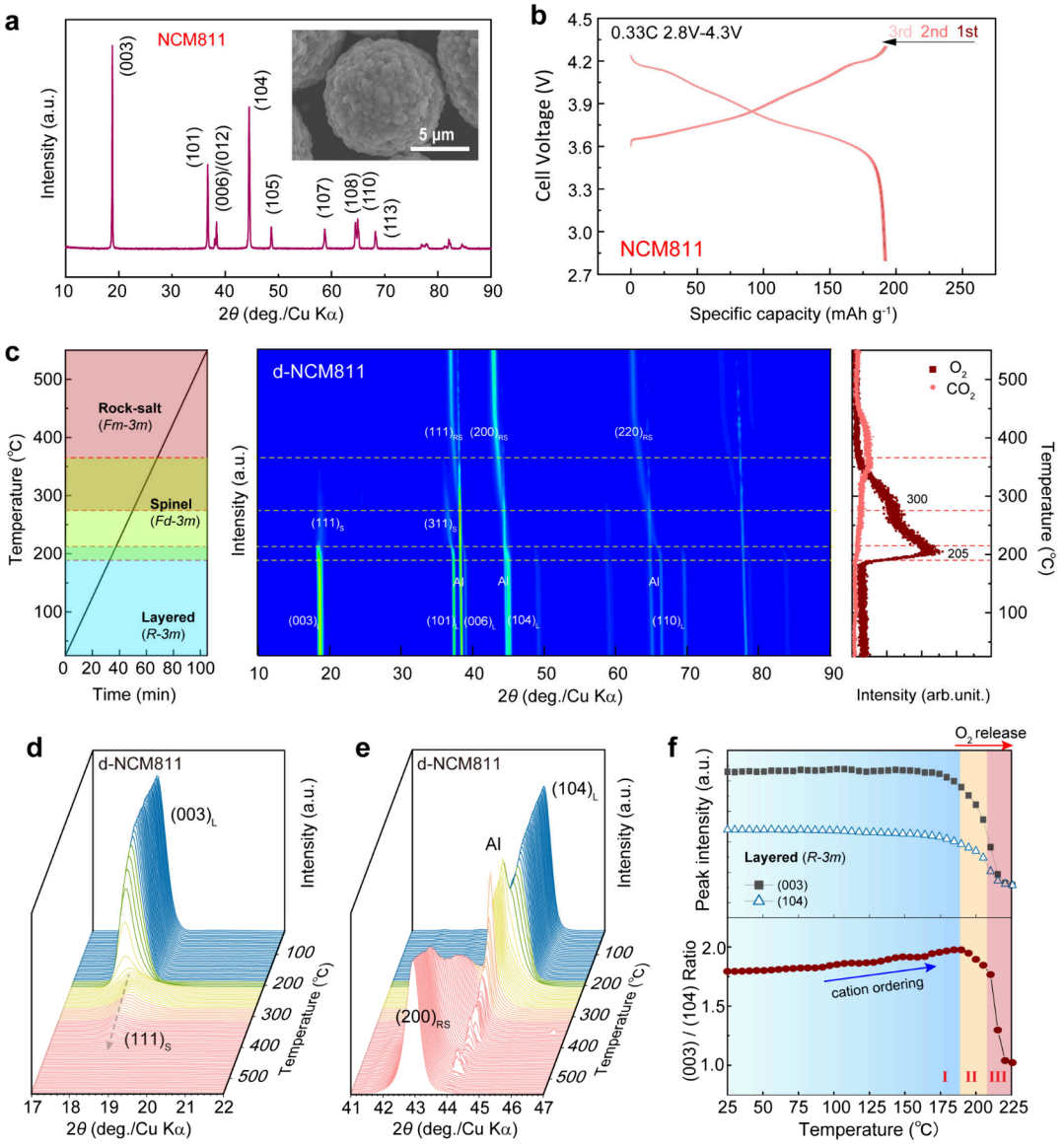

Figure 1. Structural characteristics, electrochemical performance, and*operando* XRD-OMS analysis of NCM811. (a) XRD patterns of as-synthesized NCM811. Inserts show the SEM image. (b) Galvanostatic charge−discharge curves. (c) *Operando* XRD-OMS measurements. (d, e) Enlarged XRD patterns in the ranges of 17−22° and 41−47°, highlighting the evolution of the $(003)_L$ and $(104)_L$, respectively. (f) Temperature-dependent variation of the $(003)_L$ and $(104)_L$ peak intensities below 225 °C, along with the evolution of their intensity ratio $I(003)/I(104)$. The early stage TR process was divided into three distinct phases.

where the layered framework is largely preserved. The evolution of this ratio can be divided into three regimes: (i) a slight increase at low temperature (~100−185 °C), suggesting partial relaxation of cation disorder, possibly associated with thermally activated redistribution of Ni^{2+} ions and a slight improvement in layered ordering; (ii) a maximum followed by a decrease upon the onset of O_2 release (190−210 °C) indicating increasing cation disorder during the initial O_2 evolution; and (iii) a sharp drop at higher temperatures (210−250 °C), where phase transformation dominates and intense O_2 evolution occurs. At this stage, the physical meaning of the ratio becomes limited. Overall, tracking the evolution of the $(003)_L$ and $(104)_L$ reflections reveals a transition from an ordered layered structure to a disordered and transformed state, highlighting the coupled evolution of cation distribution, structural integrity, and oxygen release during thermal decomposition of d-NCM811.

To further elucidate the role of delithiation, NCM811 electrodes were charged to 4.8 V, corresponding to a ~95% delithiation (Figure S4). *Operando* XRD-OMS measurements were conducted under isothermal conditions at 170 °C to probe the relationship between delithiation degree, phase transition kinetics, and oxygen evolution (Figure 2).

A pronounced difference in structural evolution is observed between the two states. The 4.8 V sample exhibited faster phase transformation from the layered to spinel phase, accompanied by enhanced oxygen release. Notably, the spinel $(111)_s$ reflection at ~18.5°appears after ~45 min for the 4.8 V sample, whereas a similar transformation occurs only after ~120 min in the 4.3 V sample (Figure 2d,e). These results indicate that deep delithiation accelerates the kinetic pathway of structural transformation and enhances oxygen release. Deconvolution of the $(003)_L$ reflection further reveals the coexistence of layered

https://doi.org/10.1021/acsenergylett.6c00367
ACS Energy Lett. 2026, 11, 3936−3944

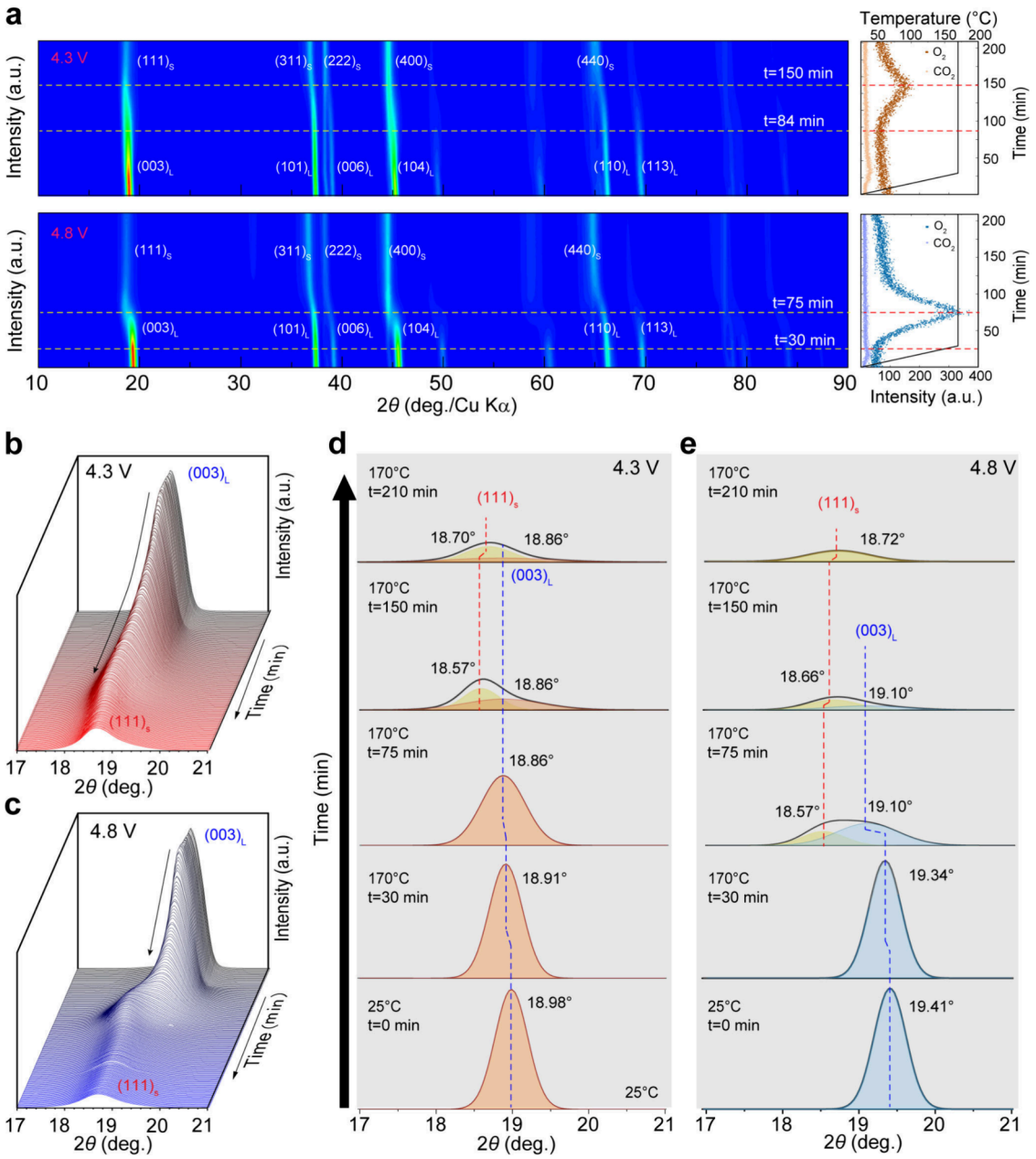

Figure 2. Structural evolution of d-NCM811 under isothermal conditions. (a) *Operando* XRD-OMS patterns of d-NCM811 samples charged to 4.3 and 4.8 V during heating and subsequent isothermal treatment at 170 °C. (b, c) Evolution of the $(003)_L$ diffraction peak for the 4.3 V (b) and 4.8 V (c) samples. (d, e) Time-resolved XRD patterns of the $(003)_L$ peak at selected time intervals during isothermal holding at 170 °C for 4.3 V (d) and 4.8 V (e), highlighting peak shifts and development of structural heterogeneity.

and spinel features during the early stage, highlighting the development of nanoscale structural heterogeneity.

We further examined how delithiation states influence the onset and severity of thermal instability. As shown in Figure 3a,b, charging to 4.8 V results in deeper Li extraction, shifting the $(003)_L$ reflection to higher 2θ and compressing the interlayer spacing to 4.56 Å, compared with 4.67 Å for the 4.3 V sample. During the initial heating stage (100−170 °C), both samples exhibit comparable *c*-axis expansion due to thermal activation, converging to a similar interlayer spacing of ∼4.75 Å.

The evolution of the $(003)_L$ peak full width at half-maximum (fwhm) provides insight into local structural heterogeneity. During isothermal treatment at 170 °C, the 4.3 V sample exhibits a gradual increase in fwhm prior to the onset of O_2 release. In contrast, the 4.8 V sample shows a more rapid and pronounced broadening that occurs concurrently with oxygen release. Here, the fwhm is interpreted qualitatively as an indicator of nanoscale structural fragmentation and reduced coherent domain size within the layered framework.[38] However, its quantitative interpretation is limited due to peak overlap with the emerging $(111)_S$ reflection during phase transformation. This interpretation is supported by high-resolution TEM observations (Figure 3c,d), which reveal the formation of nanosized spinel-like domains embedded within the layered structure in both samples, confirming the development of local structural heterogeneity.

The evolution of the $I(003)/I(104)$ ratio further correlates with oxygen-release behavior. Both samples exhibit an initial

https://doi.org/10.1021/acsenergylett.6c00367
ACS Energy Lett. 2026, 11, 3936−3944

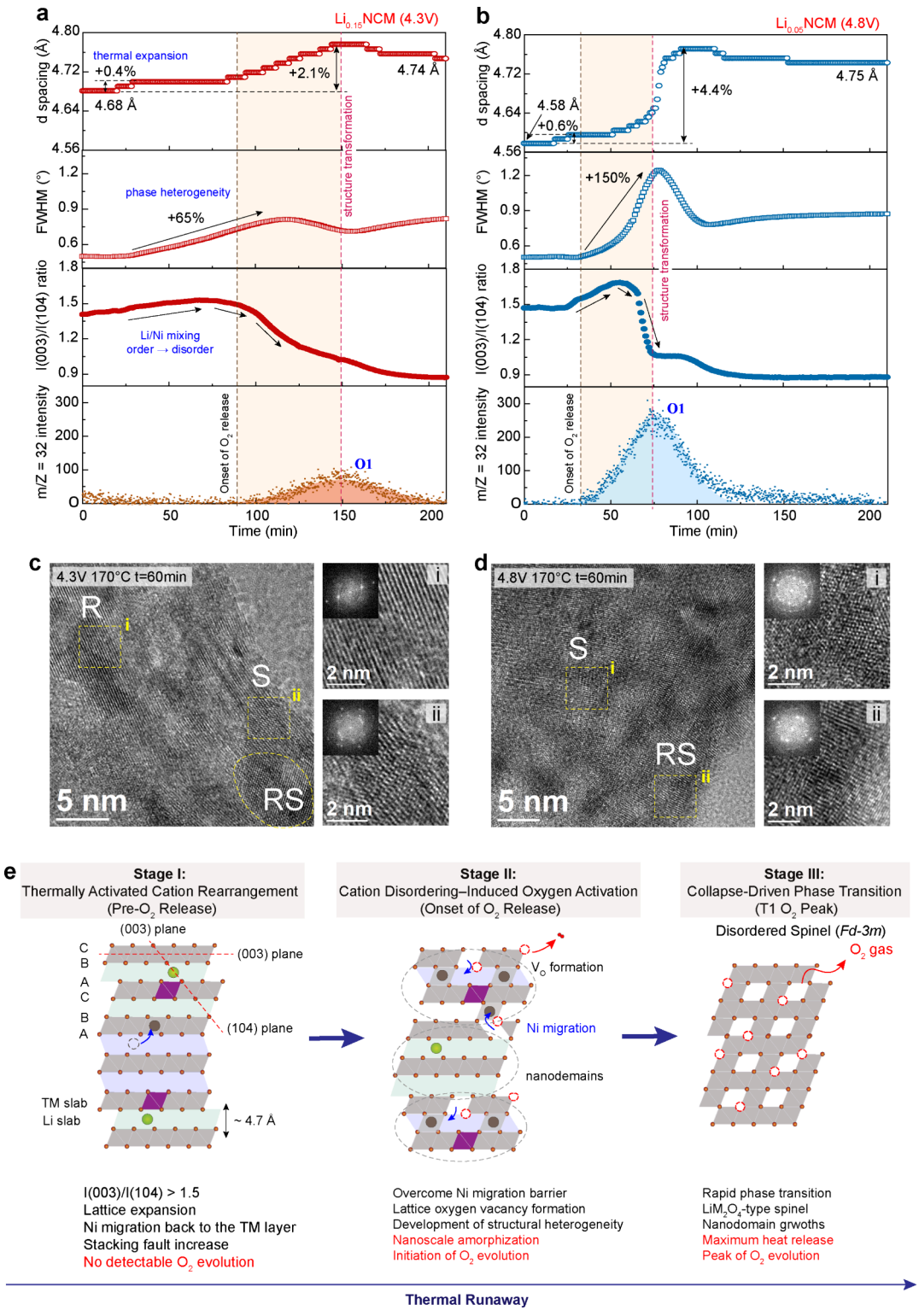

Figure 3. (a, b) Structural evolution and O_2 release behavior of samples charged to 4.3 and 4.8 V, respectively, during heating and isothermal holding at 170 °C. (c, d) High-resolution TEM images of the 4.3 V- and 4.8 V-delithiated samples with identical isothermal treatment (ramping from R.T. to 170 °C for 30 min, followed by 30 min holding at 170 °C). (e) Proposed mechanism of delithiated NCM oxide during thermal decomposition, involving cation disordering, oxygen vacancy formation, O_2 release and the layered-to-spinel phase transition.

slow increase during heating, consistent with partial cation reordering. Upon the onset of oxygen release, the ratio reaches a maximum and subsequently decreases. Notably, the kinetics differ markedly between the two states: the 4.8 V sample shows a rapid rise followed by a sharp drop in the ratio, synchronous with an intense oxygen-release event, whereas the 4.3 V sample evolves more gradually. Correspondingly, the total O_2 release from the 4.8 V sample is approximately three times higher than that of the 4.3 V counterpart (Figure S8).

https://doi.org/10.1021/acsenergylett.6c00367
ACS Energy Lett. 2026, 11, 3936−3944

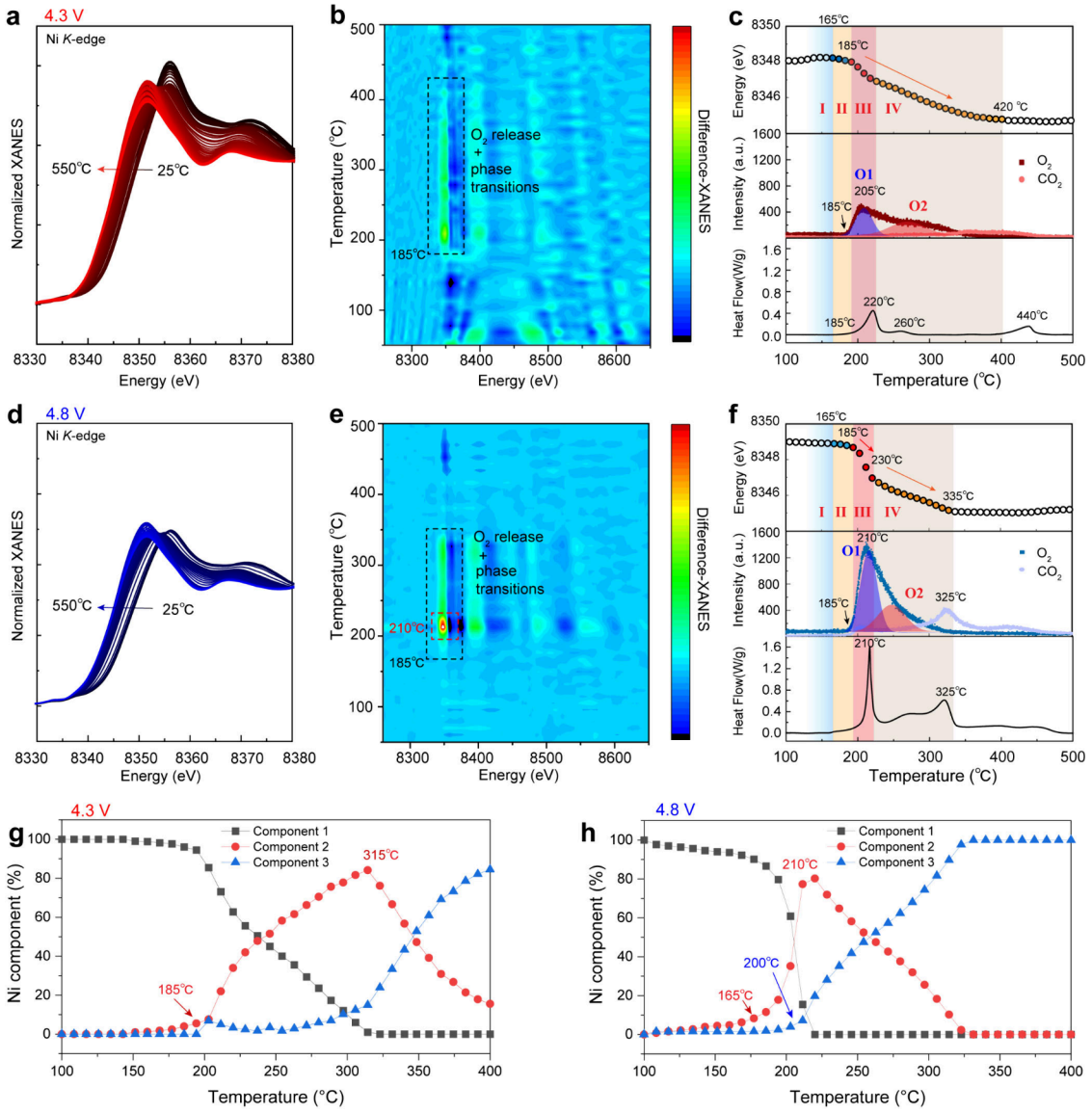

Figure 4. *Operando* Ni K-edge XAS spectra of d-NCM811 during the TR process. (a, d) Normalized Ni K-edge XANES spectra at increasing temperatures for 4.3 V (a) and 4.8 V (d) samples. (b, e) 1st derivative Ni K-edge XANES spectra. (c, f) Systematic comparison of Ni K-edge energy shifts with O_2/CO_2 release and DSC heat-flow signals. The shaded regions labeled with I−IV denote the pre-O_2 release stage, onset of O_2 release, first of O_2 release peak, and second O_2 release peak, respectively. (g, h) MCR-ALS analysis of the Ni K-edge XANES spectra during the heating process.

The schematic in Figure 3e illustrates a dynamically coupled evolution of cation migration, structural heterogeneity, and accelerated oxygen release. Increased cation disorder is observed prior to rapid structural transformation and may be associated with Ni^{2+} migration and oxygen vacancy formation in the delithiated layered structure. However, rather than following a strictly sequential pathway, these processes likely evolve concurrently within a narrow thermal window, and their precise temporal sequence cannot be unambiguously resolved. Deep delithiation further amplifies this coupled behavior. Charging to high voltages induces interlayer contraction and increased structural heterogeneity, which are commonly associated with enhanced structural susceptibility in Ni-rich cathodes, as reported in previous studies.[27,39] It should be noted that *operando* XRD primarily probes bulk structural evolution. The initial destabilization and oxygen release may originate from surface or near-surface regions, preceding the detectable bulk response.

Operando Ni K-edge XAS was performed on d-NCM811 charged to 4.3 and 4.8 V to elucidate the role of Ni redox during thermal decomposition (Figure 4). In both cases, the normalized XANES spectra (Figure 4a,d) exhibit a progressive shift of the absorption edge toward lower energies upon heating, indicating continuous reduction of Ni. The onset of average valence evolution of Ni occurs at ~185 °C for both samples.

Distinct differences are observed in the reduction kinetics. For the 4.3 V sample, the Ni K-edge gradually shifts from ~ 8348 eV to ~ 8345 eV over a broad temperature window of 185−420 °C (Figure 4c), reflecting a relatively slow and extended reduction process. In contrast, the 4.8 V sample starts from a higher initial edge position (~8349 eV), consistent with a higher initial Ni valence state, and undergoes a much more abrupt reduction within a narrower temperature window of 185−325 °C (Figure 4f). The first-derivative XANES contour map further reveals an intensified reduction event at ~210 °C for the 4.8 V sample, coinciding with the T_1 oxygen-evolution peak. At the T_1 stage,

https://doi.org/10.1021/acsenergylett.6c00367
ACS Energy Lett. 2026, 11, 3936−3944

the 4.8 V sample exhibits a rapid and pronounced Ni reduction toward lower valence states, whereas the corresponding evolution in the 4.3 V sample remains more gradual. This behavior indicates a stronger kinetic coupling between Ni redox, structural evolution, and oxygen release at higher delithiation, leading to a more synchronized and abrupt transformation process.

To further resolve the evolution of Ni valence states, multivariate curve resolution−alternating least-squares (MCR-ALS) analysis was applied to the temperature-dependent XANES data set. This approach decomposes the spectra into a set of underlying components and their relative contributions without requiring predefined reference standards, enabling identification of intermediate states during continuous redox evolution.[40] Three components were extracted, which can be assigned to high-, intermediate-, and low-valence Ni-like species based on their edge positions and spectral features (Figure 4g,h). For the 4.3 V sample, the high-valence component gradually decreases over a broad temperature range, while the intermediate component increases and then slowly transforms into the low-valence component, indicating a continuous and stepwise reduction pathway. In contrast, the 4.8 V sample shows a rapid decay of the high-valence component near ∼200−220 °C, followed by a sharp transition from intermediate to low-valence species within a narrow temperature window. This transition occurs nearly concurrently with the T_1 oxygen-release peak, indicating a highly synchronized redox process. These results demonstrate that deep delithiation shifts the Ni redox pathway from a gradual, stepwise evolution to a compressed and accelerated transition, reflecting stronger kinetic coupling among Ni reduction, structural disorder, and oxygen release. This highlights that the hazard at high voltage is not merely due to reduced thermodynamic stability, but also arises from fundamentally altered reaction pathways and kinetics.

In addition, the evolution of CO_2 is noted to closely correlate with oxygen release and structural transformation. A distinct CO_2 evolution signal is observed for the 4.8 V sample at ∼325 °C, which is both more intense and occurs at a temperature ∼100 °C lower than that of the 4.3 V sample. Under the electrolyte-free conditions employed here, the detected CO_2 is more likely associated with the thermal decomposition or oxidation of residual electrode components rather than electrolyte reactions.[41,42] Possible sources include the decomposition of surface carbonate species (e.g., Li_2CO_3), oxidation of conductive carbon, and degradation of the polymer binder (e.g., PVDF). It is possible that the formation of NiO-like rock-salt phases formed at high temperature may further catalyze and facilitate the reaction; however, the detailed mechanism remains to be clarified.

In summary, this study elucidates the intrinsic thermal decomposition behavior of Ni-rich NCM811 cathodes by integrating *operando* XRD-OMS, XAS, and DSC measurements under electrolyte-free conditions. The combined approach enables direct correlation of structural evolution, Ni redox, and gas release, providing a clear picture of cathode-driven thermal instability. Future studies employing EXAFS will enable quantitative analysis of Ni−O and Ni−TM coordination evolution.

Importantly, deep delithiation significantly amplifies this coupled behavior. Compared with moderate delithiation, the 4.8 V state exhibits stronger interlayer contraction, enhanced structural heterogeneity, and markedly accelerated Ni reduction, resulting in more abrupt oxygen release (∼3-fold higher) and accelerated phase transformation. These findings suggest that effective mitigation of thermal instability should focus on regulating this coupled evolution. Strategies such as (i) bulk doping to stabilize the layered framework and mitigate cation disorder, (ii) surface coating with thermally stable materials to suppress early stage oxygen release and surface reconstruction, and (iii) controlling the upper cutoff voltage to avoid deep delithiation are expected to reduce oxygen release and improve safety.

In practical battery systems, thermal runaway is not solely governed by cathode instability but arises from coupled reactions involving both anode and electrolyte. At relatively low temperatures, the onset of thermal failure is often initiated at the anode−electrolyte interface, where the decomposition of the solid electrolyte interphase (SEI) can release heat and gaseous species (e.g., CO_2 and hydrocarbons). As the temperature increases further, electrolyte decomposition becomes dominant, contributing significantly to gas generation and heat release. Therefore, while the present study focuses on the intrinsic thermal instability of the cathode, it should be recognized that, in full-cell systems, anode-side reactions and electrolyte decomposition can act as critical initiating and amplifying factors in thermal runaway.

■ ASSOCIATED CONTENT

Supporting Information

The Supporting Information is available free of charge at https://pubs.acs.org/doi/10.1021/acsenergylett.6c00367.

Experimental methods, experimental photos, SEM images, electrochemical characterization (including charge−discharge profiles, cycling performance), TGA analyses, *operando* XRD-OMS results, XAS spectra, etc. (PDF)

■ AUTHOR INFORMATION

Corresponding Authors

Shaofei Wang − *Fujian Science and Technology Innovation Laboratory for Energy Devices of China (21C LAB), Ningde 352100 Fujian, China*; Email: wsfwsry@163.com

Qingyu Kong − *Synchrotron Soleil, Saint-Aubin 91190, France*; orcid.org/0000-0002-3274-179X; Email: qingyu.kong@synchrotron-soleil.fr

Chunzhen Yang − *School of Materials, Sun Yat-sen University, Shenzhen 518107, China*; orcid.org/0000-0002-0487-0420; Email: yangchzh6@mail.sysu.edu.cn

Authors

Yuying Zhang − *School of Materials, Sun Yat-sen University, Shenzhen 518107, China*

Chao Wang − *School of Materials, Sun Yat-sen University, Shenzhen 518107, China*

Jihao Zhang − *Synchrotron Soleil, Saint-Aubin 91190, France*

Hanwei Liu − *School of Materials, Sun Yat-sen University, Shenzhen 518107, China*

Jianwen Wang − *School of Materials, Sun Yat-sen University, Shenzhen 518107, China*

Zhenzhong Li − *School of Materials, Sun Yat-sen University, Shenzhen 518107, China*

Wencheng Su − *School of Materials, Sun Yat-sen University, Shenzhen 518107, China*

Wei Zhou − *School of Materials, Sun Yat-sen University, Shenzhen 518107, China*

https://doi.org/10.1021/acsenergylett.6c00367
ACS Energy Lett. 2026, 11, 3936−3944

Wenbo Zhai − *Fujian Science and Technology Innovation Laboratory for Energy Devices of China (21C LAB), Ningde 352100 Fujian, China;* orcid.org/0000-0001-9384-0735
Jiahe Zang − *Fujian Science and Technology Innovation Laboratory for Energy Devices of China (21C LAB), Ningde 352100 Fujian, China*

Complete contact information is available at: https://pubs.acs.org/10.1021/acsenergylett.6c00367

Notes

The authors declare no competing financial interest.

■ ACKNOWLEDGMENTS

We thank the Shanghai Synchrotron Radiation Facility of BL02U2 (https://cstr.cn/31124.02.SSRF.BL02U2) for the assistance on XRD measurements and BL12SW (https://cstr.cn/31124.02.SSRF.BL12SW) for the assistance on PDF measurements. We acknowledge SOLEIL for the provision of synchrotron radiation facilities, and we would like to thank the SOLEIL beamline staff for the assistance (the data of X-ray absorption spectroscopy were obtained on beamline ODE under proposals 20250601 and 20250973). We also thank Kaili Li (Instrumental Analysis and Research Center, Sun Yat-sen University) for the assistance with TEM.

■ REFERENCES

(1) Wang, C.; Wang, X.; Zhang, R.; Lei, T.; Kisslinger, K.; Xin, H. L. Resolving complex intralayer transition motifs in high-Ni-content layered cathode materials for lithium-ion batteries. *Nat. Mater.* **2023**, *22* (2), 235−241.
(2) Kang, Y.; Wang, J.; Du, L.; Liu, Z.; Zou, X.; Tang, X.; Cao, Z.; Wang, C.; Xiong, D.; Shi, Q.; et al. Overcharge Investigations of $LiCoO_2$/Graphite Lithium Ion Batteries with Different Electrolytes. *ACS Appl. Energy Mater.* **2019**, *2* (12), 8615−8624.
(3) Zhang, G.; Wei, X.; Chen, S.; Zhu, J.; Han, G.; Tang, X.; Hua, W.; Dai, H.; Ye, J. Comprehensive Investigation of a Slight Overcharge on Degradation and Thermal Runaway Behavior of Lithium-Ion Batteries. *ACS Appl. Mater. Interfaces* **2021**, *13* (29), 35054−35068.
(4) Schumacher, B.; Alvarez, M. R.; Kwon, Y.; Bhai, L.; Ells, A. W.; Sullivan, J.; Munich, N.; Marbella, L. E.; Steingart, D. A. When Short-Circuits Fall Short: The Thermal Consequences of Lithium Metal Internal Short-Circuits. *ACS Energy Lett.* **2025**, *10* (9), 4074−4081.
(5) Yang, D.; Guo, H.; Wang, Y.; Wang, K. Research Progress of Lithium-Ion Battery Monitoring Technology Based on Noninvasive Magnetic Induction Sensors. *ACS Appl. Electron. Mater.* **2025**, *7* (11), 4907−4923.
(6) Hou, Q.; Li, P.; Qi, Y.; Wang, Y.; Huang, M.; Shen, C.; Xiang, H.; Li, N.; Xie, K. Temperature-Responsive Solvation of Deep Eutectic Electrolyte Enabling Mesocarbon Microbead Anode for High-Temperature Li-Ion Batteries. *ACS Energy Lett.* **2023**, *8* (9), 3649−3657.
(7) Thamodaran, P.; Murugan, V.; Sundaramurthy, D.; Sekar, K.; Maruthapillai, A.; Maruthapillai, T. Hierarchical $Na_3V_2(PO_4)_2F_3$Microsphere Cathodes for High-Temperature Li-Ion Battery Application. *ACS Omega* **2022**, *7* (30), 26523−26530.
(8) Ren, W.; Tan, R.; Qi, C.; Yang, Y.; Wang, X.; Zhao, S.; Zheng, T. Study of Polarization-Induced Strain Distribution and Mechanical Damage in Lithium-Ion Batteries. *ACS Appl. Mater. Interfaces* **2025**, *17* (50), 68579−68591.
(9) Chen, H.; Kalamaras, E.; Abaza, A.; Tripathy, Y.; Page, J.; Barai, A. Comprehensive analysis of thermal runaway and rupture of lithium-ion batteries under mechanical abuse conditions. *Appl. Energy* **2023**, *349*, 121610.
(10) Dose, W. M.; Li, W.; Temprano, I.; O'Keefe, C. A.; Mehdi, B. L.; De Volder, M. F. L.; Grey, C. P. Onset Potential for Electrolyte Oxidation and Ni-Rich Cathode Degradation in Lithium-Ion Batteries. *ACS Energy Lett.* **2022**, *7* (10), 3524−3530.
(11) Li, W. Onset of Lithium Plating in Fast-Charging Li-Ion Batteries. *ACS Energy Lett.* **2025**, *10* (4), 1596−1604.
(12) Kim, S.; Thind, A. S.; Mohanty, S. K.; Hong, J. K.; Jung, J. Y.; Park, H.; Yang, Y.; Park, M.-S.; Porwal, M. S.; Allen, E.; et al. High-Nickel Cathodes with Mechanical and Interfacial Robustness via Tailored Concentration Gradients for Stable Li-Ion Batteries. *ACS Energy Lett.* **2025**, *10* (7), 3600−3609.
(13) Feng, X.; He, X.; Ouyang, M.; Wang, L.; Lu, L.; Ren, D.; Santhanagopalan, S. A Coupled Electrochemical-Thermal Failure Model for Predicting the Thermal Runaway Behavior of Lithium-Ion Batteries. *J. Electrochem. Soc.* **2018**, *165* (16), A3748−A3765.
(14) He, Z.; Su, Y.; Luo, M.; Wei, X.; Cheng, Y.; Li, Y.; Zhang, Z.; Yan, R.; Zhao, D.; Zhang, M.; et al. Interfacial Engineering of Li-$[Ni_{0.84}Co_{0.10}Mn_{0.06}]O_2$ Cathodes for Safer Lithium-Ion Batteries. *ACS Appl. Mater. Interfaces* **2025**, *17* (22), 32340−32349.
(15) Guo, J.; Li, P.; Piccolo, F.; Jie, Y.; Jia, H.; Cao, R.; Jiao, S.; Adelhelm, P.; Xu, Y. Degradation and Failure Mechanisms of Lithium/$LiNi_xCo_yMn_{1-x-y}O_2$ Batteries. *ACS Energy Lett.* **2025**, *10* (5), 2318−2340.
(16) Lyu, P.; Liu, X.; Qu, J.; Zhao, J.; Huo, Y.; Qu, Z.; Rao, Z. Recent advances of thermal safety of lithium ion battery for energy storage. *Energy Storage Mater.* **2020**, *31*, 195−220.
(17) Wei, Z.; Liang, C.; Jiang, L.; Sun, M.; Cheng, S.; Wang, L.; Chen, S.; Fang, Z.; Li, Y.; Zhang, N.; et al. Probing the thermal degradation mechanism of polycrystalline and single-crystal $Li(Ni_{0.8}Co_{0.1}Mn_{0.1})O_2$ cathodes from the perspective of oxygen vacancy diffusion. *Energy Storage Mater.* **2023**, *56*, 495−505.
(18) Li, Y.; Liu, X.; Wang, L.; Feng, X.; Ren, D.; Wu, Y.; Xu, G.; Lu, L.; Hou, J.; Zhang, W. Thermal runaway mechanism of lithium-ion battery with $LiNi_{0.8}Mn_{0.1}Co_{0.1}O_2$ cathode materials. *Nano Energy* **2021**, *85*, 105878.
(19) Liang, Y.; Xue, H.; Zhan, M.; Cao, H.; Xu, Z.; Liu, T.; Chen, X.; Liu, J.; Li, S.; Pan, F.; et al. Stationary Oxygen Vacancy Construction toward a Superior-Performance Ultrahigh Nickel Single-Crystal Cathode. *ACS Nano* **2025**, *19* (28), 25879−25889.
(20) Liu, J.; Dong, J.; Wang, M.; Liu, N.; Wang, H.; Yan, K.; Zhang, H.; Wang, X.; Tang, R.; Lu, Y. Redox-active stabilizer-enhanced structural and thermal stability of Ni-rich cathodes via an economical blending strategy. *eTransportation* **2025**, *24*, 100428.
(21) Jung, R.; Metzger, M.; Maglia, F.; Stinner, C.; Gasteiger, H. A. Oxygen Release and Its Effect on the Cycling Stability of $LiNi_xMn_yCo_zO_2$(NMC) Cathode Materials for Li-Ion Batteries. *J. Electrochem. Soc.* **2017**, *164* (7), A1361−A1377.
(22) Kasnatscheew, J.; Röser, S.; Börner, M.; Winter, M. Do Increased Ni Contents in $LiNi_xMn_yCo_zO_2$ (NMC) Electrodes Decrease Structural and Thermal Stability of Li Ion Batteries? A Thorough Look by Consideration of the Li^+ Extraction Ratio. *ACS Appl. Energy Mater.* **2019**, *2* (11), 7733−7737.
(23) Liu, S.; Huang, S.; Zhou, Q.; Snyder, K.; Long, M. K.; Zhang, G. In Situ Measurement of Dynamic Internal Short Circuit Resistance during Nail Penetration of Lithium-Ion Cells and its Implications on Cell Robustness and Abuse Tolerance. *J. Electrochem. Soc.* **2023**, *170* (6), 060515.
(24) Yu, H.; Han, Q.; Chen, L.; Chen, L.; Jiang, H.; Li, C. Highly-Dispersed Single-Crystalline Ni-Rich Cathodes with Low Li/O Loss for High-Power and Long-Life Li-Ion Batteries. *Adv. Funct. Mater.* **2024**, *34* (51), na DOI: 10.1002/adfm.202410384.
(25) Qiu, Z.; Wang, Z.; Yuan, S. How sintering temperature affects the electrochemical performance of ultra-high nickel (Ni > 0.9) cathode material. *J. Colloid Interface Sci.* **2024**, *656*, 225−232.
(26) Kong, X.; Zhang, Y.; Li, J.; Yang, H.; Dai, P.; Zeng, J.; Zhao, J. Single-crystal structure helps enhance the thermal performance of Ni-rich layered cathode materials for lithium-ion batteries. *Chem. Eng. J.* **2022**, *434*, 134638.
(27) Liang, C.; Jiang, L.; Wei, Z.; Zhang, W.; Wang, Q.; Sun, J. Insight into the structural evolution and thermal behavior of $LiNi_{0.8}Co_{0.1}Mn_{0.1}O_2$ cathode under deep charge. *J. Energy Chem.* **2022**, *65*, 424−432.

(28) Wang, Y.; Ren, D.; Feng, X.; Wang, L.; Ouyang, M. Thermal kinetics comparison of delithiated Li[NiCoMn]O_2 cathodes. *J. Power Sources* **2021**, *514*, 230582.
(29) Nam, K. W.; Bak, S. M.; Hu, E.; Yu, X.; Zhou, Y.; Wang, X.; Wu, L.; Zhu, Y.; Chung, K. Y.; Yang, X. Q. Combining In Situ Synchrotron X-Ray Diffraction and Absorption Techniques with Transmission Electron Microscopy to Study the Origin of Thermal Instability in Overcharged Cathode Materials for Lithium-Ion Batteries. *Adv. Funct. Mater.* **2013**, *23* (8), 1047−1063.
(30) Zhang, H.; Xue, J.; Qin, Y.; Chen, J.; Wang, J.; Yu, X.; Zhang, B.; Zou, Y.; Hong, Y. H.; Li, Z.; et al. Full-Dimensional Analysis of Gaseous Products to Unlocking In Depth Thermal Runaway Mechanism of Li-Ion Batteries. *Small* **2024**, *20* (46), No. e2406110.
(31) Gachot, G.; Grugeon, S.; Eshetu, G. G.; Mathiron, D.; Ribière, P.; Armand, M.; Laruelle, S. Thermal behaviour of the lithiated-graphite/electrolyte interface through GC/MS analysis. *Electrochim. Acta* **2012**, *83*, 402−409.
(32) Li, J.; Wang, L.; Zhang, Q.; He, X. Synthesis and characterization of $LiNi_{0.6}Mn_{0.4-x}Co_xO_2$ as cathode materials for Li-ion batteries. *J. Power Sources* **2009**, *189* (1), 28−33.
(33) Kim, J.-H.; Park, K.-J.; Kim, S. J.; Yoon, C. S.; Sun, Y.-K. A method of increasing the energy density of layered Ni-rich Li-$[Ni_{1-2x}Co_xMn_x]O_2$ cathodes (x = 0.05, 0.1, 0.2). *J. Mater. Chem. A* **2019**, *7* (6), 2694−2701.
(34) Zhang, C.; Wan, J.; Li, Y.; Zheng, S.; Zhou, K.; Wang, D.; Wang, D.; Hong, C.; Gong, Z.; Yang, Y. Restraining the polarization increase of Ni-rich and low-Co cathodes upon cycling by Al-doping. *J. Mater. Chem.* **2020**, *8* (14), 6893−6901.
(35) Lee, S.; Kim, Y.; Park, C.; Kim, J.; Kim, J.-S.; Jo, H.; Lee, C. J.; Choi, S.; Seo, D.-H.; Jung, S.-K. Interplay of Cathode−Halide Solid Electrolyte in Enhancing Thermal Stability of Charged Cathode Material in All-Solid-State Batteries. *ACS Energy Lett.* **2024**, *9* (4), 1369−1380.
(36) Wang, C.; Zhang, Y.; Li, Z.; Wang, J.; Zeng, H.; Chen, J.; Liu, Y.; Li, M.; Wang, S.; Yang, C. A comprehensive understanding of the structural evolution and capacity contribution of fast-charging NCM cathodes. *J. Energy Chem.* **2026**, *114*, 183−193.
(37) Liu, P.; Yang, L.; Xiao, B.; Wang, H.; Li, L.; Ye, S.; Li, Y.; Ren, X.; Ouyang, X.; Hu, J. Revealing Lithium Battery Gas Generation for Safer Practical Applications. *Adv. Funct. Mater.* **2022**, *32* (47), na DOI: 10.1002/adfm.202208586.
(38) Park, G.-T.; Ryu, H.-H.; Park, N.-Y.; Lee, S.-B.; Sun, Y.-K. Single-Crystal vs Polycrystalline Cathodes for Lithium-Ion Batteries. *Chem. Rev.* **2025**, *125* (20), 9930−10000.
(39) Cui, Z.; Liu, C.; Wang, F.; Manthiram, A. Navigating thermal stability intricacies of high-nickel cathodes for high-energy lithium batteries. *Nature Energy* **2025**, *10* (4), 490−501.
(40) Voronov, A.; Urakawa, A.; Beek, W. v.; Tsakoumis, N. E.; Emerich, H.; Rønning, M. Multivariate curve resolution applied to in situ X-ray absorption spectroscopy data: An efficient tool for data processing and analysis. *Anal. Chim. Acta* **2014**, *840*, 20−27.
(41) Jiang, Z.; Liu, C.; Huang, L.; Zhu, S.; Zhang, X.; Wu, R.; Gong, T.; Wu, Y.; Guo, L.; Han, P.; et al. Interfacial reactions take the lead: elucidating the dominant role of cathode−electrolyte interactions in triggering thermal runaway of high-nickel lithium-ion batteries. *Energy Environ. Sci.* **2025**, *18*, 8232−8243.
(42) Jung, S. K.; Kim, H.; Song, S. H.; Lee, S.; Kim, J.; Kang, K. Unveiling the Role of Transition-Metal Ions in the Thermal Degradation of Layered Ni−Co−Mn Cathodes for Lithium Rechargeable Batteries. *Adv. Funct. Mater.* **2022**, *32* (13), na DOI: 10.1002/adfm.202108790.

https://doi.org/10.1021/acsenergylett.6c00367
ACS Energy Lett. 2026, 11, 3936−3944